



Airfoil-like mechanics generate thrust on the anterior body of swimming fishes

Kelsey N. Lucas^{a,1,2} , George V. Lauder^a , and Eric D. Tytell^b

^aOrganismic and Evolutionary Biology, Harvard University, Cambridge, MA 02138; and ^bDepartment of Biology, Tufts University, Medford, MA 02155

Edited by John Long, Vassar College, Poughkeepsie, NY and accepted by Editorial Board Member Neil H. Shubin March 18, 2020 (received for review November 8, 2019)

The anterior body of many fishes is shaped like an airfoil turned on its side. With an oscillating angle to the swimming direction, such an airfoil experiences negative pressure due to both its shape and pitching movements. This negative pressure acts as thrust forces on the anterior body. Here, we apply a high-resolution, pressure-based approach to describe how two fishes, bluegill sunfish (*Lepomis macrochirus* Rafinesque) and brook trout (*Salvelinus fontinalis* Mitchell), swimming in the carangiform mode, the most common fish swimming mode, generate thrust on their anterior bodies using leading-edge suction mechanics, much like an airfoil. These mechanics contrast with those previously reported in lampreys—anguilliform swimmers—which produce thrust with negative pressure but do so through undulatory mechanics. The thrust produced on the anterior bodies of these carangiform swimmers through negative pressure comprises 28% of the total thrust produced over the body and caudal fin, substantially decreasing the net drag on the anterior body. On the posterior region, subtle differences in body shape and kinematics allow trout to produce more thrust than bluegill, suggesting that they may swim more effectively. Despite the large phylogenetic distance between these species, and differences near the tail, the pressure profiles around the anterior body are similar. We suggest that such airfoil-like mechanics are highly efficient, because they require very little movement and therefore relatively little active muscular energy, and may be used by a wide range of fishes since many species have appropriately shaped bodies.

fish swimming | carangiform | pressure | force | airfoil

It has long been appreciated that the shape of many fishes resembles a streamlined body (1–4). In particular, the two-dimensional (2D) horizontal cross-section through many fishes is similar in shape to modern airfoil profiles designed to minimize drag (3). Because nearly all aspects of a fish's life depend on how well it swims, it has been suggested that this shape represents an evolutionary optimization to minimize drag for economical swimming (1). In general, swimming performance is linked to the evolution of fish body forms and movement patterns (5–10). For fishes that swim fast or migrate long distances, even small energy savings may be important.

However, along with reducing drag, an airfoil can directly generate propulsive forces by virtue of their shape and an effect called leading-edge suction. Due to its shape, an airfoil will generate a positive (above ambient) pressure stagnation point near its leading edge as flow divides to move along either side of the foil (3, 4, 11, 12). Then, the airfoil generates negative (below ambient) pressure over much of its length (Fig. 1*B*, and similar to the time-averaged pressure in Fig. 1*A*) (3, 4, 11–13). Since pressure produces a force perpendicular to the surface, negative pressure along the leading portion of the foil (~5 to 40% in Fig. 1*A* and *B*) will contribute to thrust because the surface there is angled forward (illustrated in Fig. 1*B*) (4, 11, 14). Airfoils also produce thrust on their anterior regions through leading-edge suction when they are at an angle to the flow (12, 15, 16). When the airfoil is angled, the stagnation point and region of positive pressure is not directly on the tip of the airfoil (Fig. 1*A*

and *C*) (15, 16). When the positive pressure deflects to one side, negative pressure moves forward to act more anteriorly on the opposite side (compare Fig. 1*B* and *C*) (15, 16). This area of negative pressure, positioned alongside forward-facing surfaces near the airfoil's leading edge, acts as local forces with small thrust components in a mechanism called leading-edge suction (Fig. 1*C*) (11, 12, 14–16).

If a fish's body resembles an airfoil turned on its side, then we might expect that the anterior body might similarly produce thrust due to its shape and movements. Fishes that swim by primarily undulating the posterior half or less of their bodies in a range of patterns broadly classified as “carangiform” characteristically have airfoil-like bodies. However, while it has long been recognized that the airfoil-like shape of a carangiform swimmer is crucial for drag reduction (1, 4, 14, 17, 18), particularly due to the tapered posterior body that helps to prevent flow separation (3, 11, 12, 19), the potential for thrust production on the anterior body of a swimming fish has not been examined experimentally. Some previous researchers hypothesized that fish could benefit from this effect, with local thrust greatly reducing the impact of the net drag expected on a carangiform swimmer's anterior body (20). Indeed, in computational models, one can see areas of

Significance

Many fishes have bodies shaped like a low-drag airfoil, with a rounded leading edge and a smoothly tapered trailing region, and move like an airfoil pitching at a small angle. This shape reduces drag, but its significance for thrust production by fishes has not been investigated experimentally. By quantifying body surface pressures and forces during swimming, we find that the anterior body shape and movements allow fishes to produce thrust in the same way as an oscillating airfoil. This work helps us to understand how the streamlined body shape of fishes contributes not only to reducing drag but also directly to propulsion, and by quantitatively linking form and function, leads to a more complete understanding fish evolution and ecology.

Author contributions: K.N.L. and G.V.L. designed research; K.N.L. performed research; G.V.L. provided equipment and fish care; K.N.L. and E.D.T. analyzed data; and K.N.L., G.V.L., and E.D.T. wrote the paper.

The authors declare no competing interest

This article is a PNAS Direct Submission. J.L. is a guest editor invited by the Editorial Board.

Published under the PNAS license.

Data deposition: The fish swimming data files and statistical analyses reported in this paper have been deposited in the Harvard Dataverse, <https://doi.org/10.7910/DVN/1SOLNG> (“Surface pressure and swimming force calculation data for bluegill and trout steadily swimming at 2.5 L/s” dataset). The scripts used for data processing reported in this paper have been deposited in GitHub, <https://github.com/kelseynlucas/Forces-on-carangiform-swimmers>.

¹Present address: School for Environment and Sustainability, University of Michigan, Ann Arbor, MI 48109.

²To whom correspondence may be addressed. Email: kelsey.n.lucas@gmail.com.

This article contains supporting information online at <https://www.pnas.org/lookup/suppl/doi:10.1073/pnas.1919055117/-DCSupplemental>.

First published April 27, 2020.

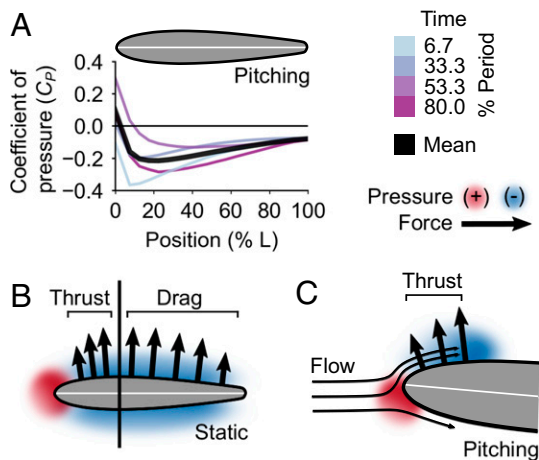


Fig. 1. Physical mechanics of airfoils. (A) Coefficient of pressure (c_p) along one side of a NACA 0015 airfoil with a rounded trailing edge pitching at reduced frequency 0.2, about 0° mean angle of attack, with an amplitude of $\pm 5^\circ$ (13). Colors indicate instantaneous pressure profiles, while the thick black line represents the time-averaged mean. (B) Pressure gradients around an airfoil (here, static at 0° angle of attack) act perpendicularly to the surface and can contribute to thrust or drag forces based on the orientation of the surface. (C) Leading-edge suction occurs when pitching movements of the airfoil shift the stagnation point and positive pressure to one side, allowing negative pressure to act more anteriorly on the opposite side (11, 12, 14–16). For clarity, in B and C, only negative-pressure forces on one side of the airfoil are shown.

negative pressure on the anterior body (21, 22), but this effect has never been studied systematically or in living fishes. We therefore used a recent set of tools (23, 24) to quantify the pressure and forces produced during swimming for two fish species that both have airfoil-shaped anterior bodies, bluegill sunfish (*Lepomis macrochirus* Rafinesque) and brook trout (*Salvelinus fontinalis* Mitchell), at high temporal and spatial resolution, the first such experimental test for negative-pressure thrust production in living carangiform swimmers.

It is known that some fishes can produce negative pressures during swimming. Specifically, Gemmell et al. (25, 26) quantified the pressure distribution around larval lampreys and found that they produce negative pressures along the anterior parts of their bodies, resulting in thrust forces. In essence, larval lampreys suck themselves forward.

The negative pressures produced by larval lampreys are not due to airfoil-like mechanics. Instead, they are likely due to the high-amplitude movements of their bodies (26), a pattern called “anguilliform” swimming, which is used primarily by a few eel-like elongate fish species (17, 27). Many anguilliform swimmers undulate a large fraction of their bodies at high amplitude, which is different from the pattern seen in many other fishes, which use the carangiform mode (17, 27). Moreover, larval lampreys use unusually high amplitudes when they swim, even compared to adult lampreys (28). It is not known whether negative-pressure thrust is a quirk of their specific swimming mode, or whether such negative pressures can be produced by other fish species and swimming modes, particularly the carangiform mode, the most common swimming mode (27, 29).

We find that both bluegill sunfish and brook trout produce negative-pressure thrust on their anterior bodies, but they do it using a very different mechanism from larval lampreys: the combination of their airfoil-shaped bodies and leading-edge suction. Our descriptions of pressure and force along the body also enable us to begin to tease apart how subtle differences in shape and movement affect swimming in a broader context. The carangiform swimming pattern belies the subtler but substantial

variation in forms, movements, and ecological roles that exists within this mode (7, 20, 29, 30). For example, bluegill have a relatively deep trunk and shallow peduncle when viewed laterally, undulate only the posterior third of their bodies at a large amplitude (20), and are found in lakes, where they generally tend to hover or swim slowly (31, 32). In comparison, brook trout have a relatively shallower trunk and deeper peduncle, undulate slightly more of their body at large amplitude (20), and live in running water where they swim often and at high speeds (33, 34). These differences are sufficiently large that, based on undulation amplitude alone, sometimes these fishes are considered examples of the two different carangiform subtypes—true carangiform (bluegill) and subcarangiform (trout) (30). These species differ in body shape and swimming movements; we identify subtle features of the swimming kinematics that lead to differences in their force production.

More broadly, our understanding of fish evolution and ecology is limited by the lack of comprehensive descriptions of swimming force production. Such descriptions, such as those presented here, will enable us to evaluate the strength of the relationships between body shape, movements, and swimming abilities. By helping to identify specific selection pressures underlying the diversity of modern fish forms, we can make predictions about the roles of different fishes within a given assemblage—species co-occurring in the same water body (7, 14, 18, 20). This understanding of the links between form and function in fishes can offer potential solutions for current underwater vehicle design challenges (35–37), such as producing animal-like vehicles less disruptive to aquatic life, enhancing swimming efficiency of biomimetic vehicles for longer-term deployments, or improving maneuvering capabilities for navigating environments with complex physical structure.

Results

We measured fluid flow patterns in a horizontal plane around five bluegill sunfish (9.3- to 11.5-cm total length L) and three brook trout (10.0- to 11.0-cm total length) using standard digital particle image velocimetry (38). Individual fishes swam in a flow tunnel at $2.5 L \cdot s^{-1}$, which corresponded to Reynolds numbers ($Re = \rho u L / \mu$, where ρ is water density, u is flow velocity, L is fish body length, and μ is water’s dynamic viscosity) (17) of 20,000 to 30,000. Tailbeat frequencies were 4.9 ± 0.5 Hz for bluegill and 4.7 ± 1.0 Hz for trout, corresponding to Strouhal numbers ($St = fA/u$, where f is tailbeat frequency and A is peak-to-peak tailbeat amplitude) (22) of 0.156 to 0.404 and reduced frequencies $f^* = fL/u$ (17) of 2.0 ± 0.2 for bluegill and 2.1 ± 0.4 for trout.

The Anterior Body Makes Small Movements. For both species, the amplitude (the distance from the center line to maximum excursion on one side or the other) was very small in the anterior body and increased in more posterior segments (Fig. 2A and B). In segments 1 to 3 (0 to 40% L), the amplitude was less than 2% L for both species, and only increased to 3% L in segment 4 of trout and segment 5 of bluegill, before increasing to 6% L or more in the posterior-most segments (Fig. 2C and D). In comparison, the body’s maximum width was $\sim 13\%$ L for both species (Fig. 2A and B). Likewise, the body angle made with the fish’s trajectory was less than 5° in segments 1 to 3 and increased over the posterior body to 30 to 40° (Fig. 2E and F).

The Anterior Body Generates Negative Pressures. The body and tail motion swept fluid alongside the anterior body, like an airfoil, before accelerating the fluid alongside the posterior body and entraining it into vortices that were shed as the tail reached maximum excursion and changed direction (Movies S1 and S2). This led to pressure fields (Fig. 3A and B and Movies S3 and S4) with a region of strong positive pressure upstream of the snout,

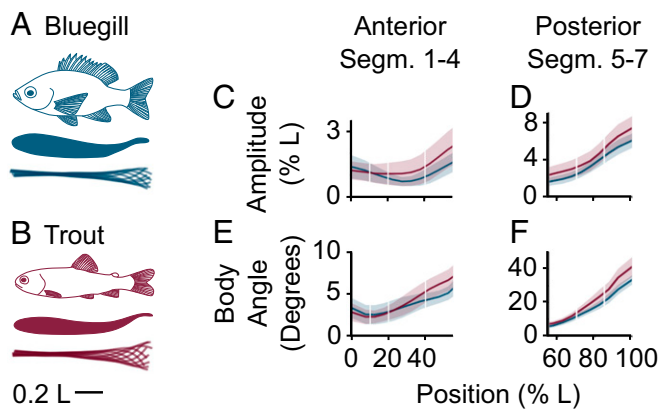


Fig. 2. Bluegill and trout are carangiform swimmers. Overall midline kinematics for bluegill (A) and trout (B) swimming at $2.5 L \cdot s^{-1}$ indicate they are carangiform swimmers. Subtle differences between carangiform subtypes are visible through comparison of amplitude (C and D) and body angle (E and F) for anterior (C and E) and posterior (D and F) segments (Segm.), where segments are defined as in Fig. 3.

negative pressure along most of the anterior body, and oscillating positive- and negative-pressure gradients along the posterior body and caudal fin.

To control for the difference in swimming speed among the fishes, we computed pressure coefficients: $C_P = P/(0.5\rho v^2)$, where P is pressure. Fig. 4 shows the instantaneous pressure coefficients along one side of the body, along with the time-averaged value.

The overall shapes of the pressure coefficient profiles had three important differences across the species (Fig. 4). First, the region of positive pressure on the snout was smaller in trout, resulting in negative pressure developing more anteriorly (Fig. 3 A and B and [Movies S3](#) and [S4](#)). Second, bluegill often had larger magnitude negative-pressure coefficients in the mid-body (10 to 55% L) than trout, but trout had larger positive- and negative-pressure coefficients in the posterior body (55 to 100% L). Finally, for both species, pressure shifted from negative in the midbody to positive near the tail, but for trout, this shift at times occurred more anteriorly (particularly at time $t = 80.0\%$ of the tailbeat cycle in Fig. 4).

The instantaneous pressure coefficients often differed greatly from the mean profiles (Fig. 4). Notably, the location where pressure coefficient changes sign from negative to positive shifted in the midbody region, and at times, a second area of negative pressure appeared on the posterior body (e.g., time $t = 53.3\%$ of the tailbeat cycle; Fig. 4).

Negative Pressure Produces Thrust on the Anterior Body. The shifting pressure gradients, combined with the body kinematics, led to complex spatial and temporal patterns of axial forces (Figs. 3 C and D and 5 and [Movies S5](#) and [S6](#)). Both positive and negative pressure could produce thrust or drag, depending on the orientation of the body (Fig. 1B). Thus, there were four types of forces: thrust due to positive pressure, thrust due to negative pressure, drag due to positive pressure, and drag due to negative pressure (Figs. 3 and 5). For bluegill, mean thrust forces were 1.3 ± 0.5 mN. Trout produced a mean thrust of 1.5 ± 0.4 mN. All values were on the same order of magnitude as previous estimates from wake analyses (39, 40).

Fig. 5 shows the spatial and temporal patterns of these four forces in the two species, along with time-averaged values, on one side of the fishes' bodies. Again, to control for the difference in body shape and swimming speed among species, forces were normalized to coefficients: $C_F = F/(0.5\rho S v^2)$, where F is force

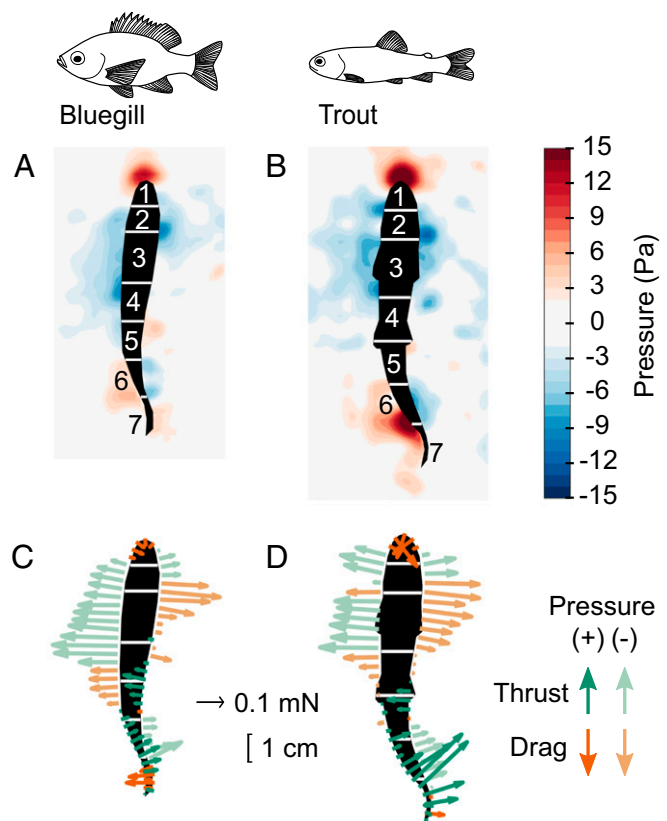


Fig. 3. Undulatory swimming motions produce spatially and temporally complex patterns of pressure and forces. Panels show pressure fields (A and B) and estimated force vectors (C and D) for bluegill sunfish and trout swimming steadily at $2.5 L \cdot s^{-1}$. Numbering for body segments used throughout are given in A and B, and the white lines indicate segment boundaries. For clarity, only every third force vector is plotted in C and D.

and S is lateral surface area. Most of the mean coefficients for axial force subtypes were significantly different between bluegill and trout (Fig. 5 C and D). Traces showing mean force coefficients summed across both sides of the body, as well as mean streamwise (total, rather than broken down by subtype) and lateral force coefficients on each body segment, are available in [SI Appendix, Figs. S1–S3](#).

Spatially, the anterior body's angle (Fig. 2 E and F) combined with the negative pressures led to thrust on the anterior body and the tail, while positive pressures contributed to thrust only in posterior segments (Fig. 5). On the tip of the snout, positive pressure produced net drag (dark orange), but slightly more posteriorly, the pressure became negative, producing negative-pressure thrust (light green). This shift occurred in segment 1 (0 to 10% L) for trout but in segment 2 (10 to 20% L) for bluegill, and in both species, negative pressures in segment 2 (10 to 20% L) produced thrust. Positive-pressure thrust coefficients (dark green) occurred in segments 4 to 7 (40 to 100% L) and increased from anterior to posterior. Negative-pressure thrust (light green) also occurred in the most posterior segments (segments 6 to 7, 70 to 100% L). Positive-pressure drag (dark orange) was only present in segments 1 (0 to 10% L) and 7 (85 to 100% L). Negative-pressure drag (light orange) was concentrated in the midbody (segments 3 to 5, 20 to 70% L).

Trout Produce Positive-Pressure Thrust More Anteriorly than Bluegill.

The pattern of axial force coefficients along the body was different among species, depending on whether force was a thrust

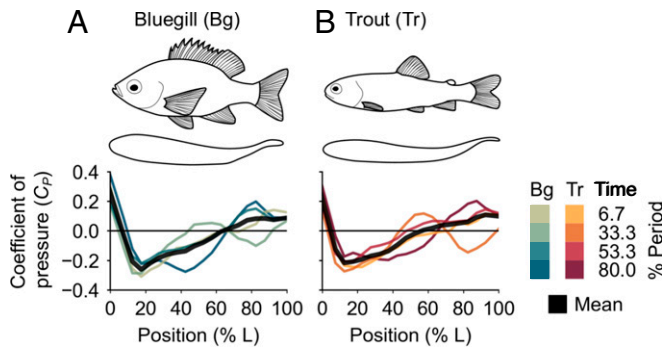


Fig. 4. Profiles of pressure coefficient C_p along the body vary over the tailbeat period. Colored traces show instantaneous profiles for bluegill (A) and trout (B) along the one side of the body, while thick black traces show the time-averaged mean. Line art above the charts represents lateral (Top) and dorsal (Bottom) views of the fishes.

or drag force, and whether the force came from positive or negative pressure (linear mixed-model ANOVAs: significant four-way interaction among species, force type, pressure type, and body segment; numerator DF = 6, denominator DF = 610, $F = 4.1312$, $P = 0.0004$). Where the two species had significantly different force coefficients, trout had larger magnitudes than bluegill, except for negative-pressure drag in segment 5 (55 to 70% L; Fig. 5).

Fig. 6 compares within a species the different force types in three posterior segments that are functionally important. For bluegill, segment 4 (40 to 55% L) had significantly more drag than thrust (Fig. 6A), but in trout these two forces were equal (Fig. 6B). In segment 5 (55 to 70% L), the pattern shifted; trout produced more thrust than drag (Fig. 6B), but in bluegill they were equal (Fig. 6A). Thus, bluegill produced net drag in segment 4 and no net force in segment 5, while trout produced no net force in segment 4 and thrust in segment 5 (Fig. 6 and *SI Appendix*, Fig. S2). Moreover, trout produced the same amount of lateral force as bluegill in segment 5 (*SI Appendix*, Fig. S3). The kinematics of these segments were different in the two species: trout had higher amplitudes and higher angle to the horizontal (Fig. 2).

We approximate hydrodynamic Froude efficiency η , the ratio of useful power to total power (17), as $\eta = \sum_i (\mathbf{F}_{T,i} \cdot \mathbf{v}_i) / \sum_i |\mathbf{F}_i \cdot \mathbf{v}_i|$, where $\mathbf{F}_{T,i}$ is the thrust force vector, \mathbf{F}_i is the total force vector, and \mathbf{v}_i is the total velocity relative to the flow (including both side to side motion and the flow velocity) each on segment i . Based on this estimate, trout swim with an efficiency of $29.5 \pm 1.9\%$, compared to $26.6 \pm 1.0\%$ in bluegill (mean \pm SE; no significant difference across species; $P = 0.142$).

Discussion

Many mechanical explanations of fish swimming emphasize that fishes push fluid behind them as they swim, creating areas of positive pressure on the body that push the fish forward as thrust forces (17, 25, 37). Thus, the recent discovery that larval lampreys rely substantially on negative pressure for thrust production (25) pointed to the underappreciated role of negative pressure in fish locomotion. Here, we present experimental data to show that the shape and oscillation of the airfoil-like body, common to many species of fishes, results in negative pressures that contribute significantly to thrust through a different mechanism than that used by larval lampreys. Using recent techniques for temporally and spatially resolved pressure and force measurements (23, 24), we find that, like in lampreys, negative pressure contributes significantly to swimming forces along a carangiform swimmer's body (Fig. 5), producing 39% of the total

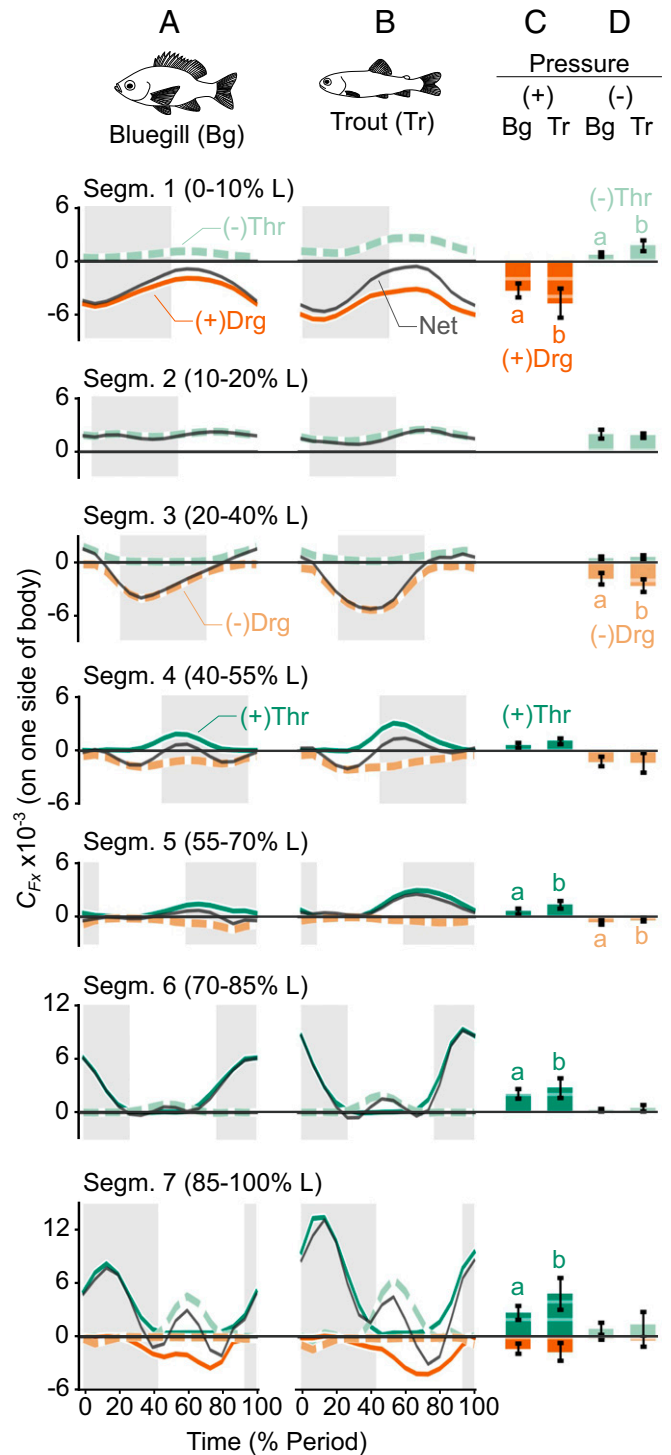


Fig. 5. Thrust and drag arise from both positive and negative pressure in time- and space-dependent patterns. A and B compare phase-resolved forces for bluegill (A) and trout (B) for seven segments (Segm.) along one side of the body. Letters indicate where significant differences in force magnitude were detected across species ($P < 0.05$). The shaded region in the background indicates the times when the body segment moved from left to right, from peak amplitude to peak amplitude. C and D compare mean thrust (Thr) and drag (Drg) forces arising from positive (C) (+) or negative (D) (-) pressure. When lines or bars are not shown, it means that both species' mean force coefficients were effectively zero ($C_{Fx} < 5\%$ total C_{Fx} for that force type).

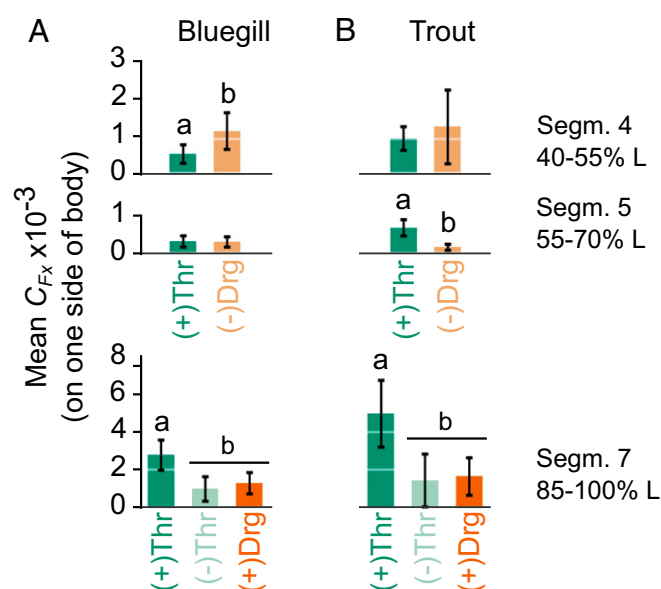


Fig. 6. Bluegill and trout use their bodies differently to produce swimming forces. Comparison of thrust (Thr) and drag (Drg) forces from positive (+) and negative (-) pressure on one side of the body at posterior body segments (Segm.) for bluegill (A) and trout (B). Letters indicate significant differences between force types within a species ($P < 0.05$).

thrust over the whole body. Unlike lampreys, however, most of the negative-pressure thrust produced by carangiform swimmers arises not from high-amplitude swimming motions, but rather from the airfoil-like mechanics of the anterior body. Negative pressure acting on the anterior body produces 28% of total thrust. For comparison, the anterior body produces 36% of the total thrust when positive- and negative-pressure contributions are combined.

In addition, the high spatial and temporal resolution of our methods allows us to determine how small differences in kinematics among swimmers produced significant differences in forces (Figs. 2 and 6). Specifically, small differences in the body amplitude and angle of the posterior body, in combination with differences in lateral body depth profiles, allowed trout to produce higher thrust forces without increasing lateral forces and so may allow them to swim more effectively than bluegill. Thus, control of pressure gradients via both the airfoil-like shape of the anterior body and the kinematics of the posterior body are important for the effective development of swimming forces.

Thrust on the Posterior Body Comes from Both Positive and Negative Pressure. About two-thirds of the thrust comes from a familiar undulatory mechanism, as predicted by earlier studies (17, 20, 41, 42), relying on both positive and negative pressure in the posterior body. Time-averaged pressure profiles were previously measured by Dubois et al. (42), and theirs and ours both generally resembled the time-averaged pressure pattern on a pitching airfoil (Fig. 14), especially on the anterior half of the body. Our profiles from the posterior body only look like theirs when averaged over a tailbeat cycle (Fig. 4). In instantaneous pressure profiles, pressure changes sign depending on location on the body and time within the tailbeat cycle (Fig. 4), resembling the distinct, alternating “pressure” (positive pressure) and “suction” (negative pressure) regions alongside the posterior body posited by Müller et al. (41) and found on the posterior bodies in computational models of carangiform swimmers (21, 22). This contrasts with the uniformly negative pressure on the posterior portion of a pitching airfoil (Fig. 14). In particular, the

caudal fin (segment 7, 85 to 100% L) experienced three forces: positive-pressure thrust on the leading side of the lateral motion, negative-pressure thrust on the trailing side, and positive-pressure drag on the trailing side (Fig. 5). Together, these three forces produce a peak in thrust every time the caudal fin travels between peak excursions and near-zero forces as the caudal fin changes direction (Fig. 5 and *SI Appendix*, Fig. S1). Dubois et al. (42–44) were not unaware of these effects; they noted that pressures fluctuated on some parts of the fish’s body in rhythm with the tailbeat, that there were negative pressures on the trailing side of the caudal fin, and that the caudal fin produces some drag, observations that all agree with ours.

We suggest that the actions of all three of these forces are necessary to create the shape of the characteristic double-peak pattern of thrust production over a tailbeat cycle (20, 29, 43–45). The positive pressure acting on the leading side of the caudal fin (segment 7, 85 to 100% L) is the primary source of thrust, leading to the magnitude of peak forces in the net force curves (Fig. 5 A and B and *SI Appendix*, Fig. S1), since the magnitude of negative-pressure thrust is equal to the magnitude of positive-pressure drag (Fig. 6). This, again, agrees with computational models of carangiform swimming, where thrust was concentrated on the caudal region (21, 22). However, the timing of the peaks in positive-pressure thrust on the leading side of the caudal fin and in negative-pressure thrust on the trailing side differs (Fig. 5 A and B and *SI Appendix*, Fig. S1). In addition, the staggered timing of negative-pressure thrust and positive-pressure drag on the caudal fin—with the thrust acting first and quickly, and the drag acting second and slowly (Fig. 5 A and B)—influences the timing of peak thrust and the shape of the net force curve on the caudal fin. This influence is visible when comparing across bluegill and trout; in trout, the negative-pressure thrust peak occurs earlier, leading to net force curves with different shapes across species (Fig. 5 A and B and *SI Appendix*, Fig. S1).

The implication here is that a fish’s control of pressure gradients around its caudal fin through adjustments to caudal fin shape or body kinematics may be vital for tuning thrust production on the posterior body. This agrees with Müller et al.’s (41, 46) hypothesis that fish can make small adjustments to their kinematics to control flow around the body and fine-tune their swimming performance, and further, this points to specific features—caudal fin shape and posterior body kinematics—that could have been influenced by selection on swimming abilities over the course of fish evolution.

It is important to note that the patterns of force production we describe here only reflect steady swimming. Presumably, timing, magnitude, and location of forces, in addition to the relative role of positive and negative pressure, could all change during accelerations. For example, many carangiform swimmers, including bluegill, have larger head and tail oscillation amplitudes and larger tailbeat frequencies during accelerations (39, 47), leading to larger added masses and larger total forces (39). Interestingly, in bluegill (39) but not trout (47), these increases occur without substantially redirecting the net thrust forces relative to steady swimming, suggesting that there are differences in the force production mechanics among species and across behaviors like steady swimming and accelerations.

Trout May Produce Swimming Forces More Effectively than Bluegill. From their lifestyles, we might hypothesize that bluegill, which generally hover or swim slowly in still water or slowly flowing streams (20, 31, 32), do not produce thrust as effectively as trout, which spend much of their lives swimming (20, 33, 34), even though both swim in a similar way. If this hypothesis is correct, then what aspects of kinematics or body morphology in trout lead to more effective swimming? Answering questions like these, both within and across swimming modes, would allow us to

evaluate the strength of relationships between swimming abilities, morphology, and kinematics, and further, identify specific selection pressures that may have led to modern fish forms. Our pressure measurements allow us to approximate hydrodynamic Froude efficiency, the ratio of useful and total power. We find that the Froude efficiency is 2.9% higher in trout than bluegill. Earlier predictions likewise suggest that trout may have higher Froude efficiencies than bluegill (20). The difference we observe in efficiency, while not significant ($P = 0.142$), may point toward functional differences in thrust production between trout and bluegill. Froude efficiency is only a mechanical efficiency and does not account for potential differences in metabolic rates (1), but even such small differences in efficiency could lead to significant energy savings over the long bouts of continuous swimming typical of a trout's lifestyle (20, 33, 34).

Indeed, we hypothesize that the subtle differences in kinematics and body shape among the species are functionally meaningful. The midbody (segments 4 to 5, 40 to 70% L), where forces transition from drag to thrust, is the most functionally relevant. In bluegill, the transition from drag to thrust occurred on body segment 5 (55 to 70% L), where the net force coefficient was near zero (Fig. 6A and *SI Appendix*, Fig. S2). In contrast, in trout, this transition occurred more anteriorly in segment 4 (40 to 55% L), with segment 5 (55 to 70% L) clearly producing thrust (Fig. 6B and *SI Appendix*, Fig. S2).

These differences seem to reflect kinematic differences among the species: trout are sometimes classified as “subcarangiform” swimmers, which have higher amplitude undulations more anteriorly on their body than “true-carangiform” swimmers like bluegill (Fig. 2 A–C) (20). First, the more anterior transition to undulatory motion in trout means that the development of thrust-producing positive-pressure gradients occurs more anteriorly, too (Fig. 4, time $t = 53.3$ and 80% of the tailbeat cycle). Second, in trout, these more posterior segments make a larger angle to the swimming trajectory (Fig. 2 E and F), directing the forces more toward thrust than lateral forces. Indeed, the ratio of axial to lateral force coefficients is much larger in this segment in trout than in bluegill (0.33 in trout and 0.06 in bluegill) (Fig. 5 and *SI Appendix*, Figs. S2 and S3).

As a whole, our results suggest that trout are producing swimming force more effectively than bluegill. This is because they produce higher thrust forces than bluegill and use more of their body to produce thrust. However, although trout are undulating at larger amplitudes, the lateral forces they produce are no different from or are less than (segment 4, 40 to 55% L) those of bluegill (*SI Appendix*, Fig. S3). Since lateral forces are wasted effort (part of the denominator in Froude efficiency), these larger body undulations do not appear to be incurring additional costs for the trout. We suggest that this is due to trout's shallower body depth profile. While a full analysis of morphology, lateral forces, and swimming efficiency is beyond the scope of this study, these findings suggest that an examination of subtle differences across carangiform swimmers is a promising direction for future work linking form and function in fishes.

The Anterior Body Produces Thrust due to Airfoil-Like Mechanics. Despite the differences in force distribution in posterior segments, the overall pattern of pressure and forces in the anterior body is quite similar across bluegill and trout and much like that over an airfoil. The reduced frequency of oscillation is fairly large (~ 2 for both species), suggesting that oscillatory mechanics might be more important than airfoil-like mechanics. However, we find that the pressure distribution on the anterior body is very similar to an airfoil at a constant angle of attack (reduced frequency of 0) (48) or a pitching airfoil at a much lower reduced frequency (0.2 in Fig. 1A) (13).

For both fishes, the cross-sectional shape of the anterior body is close to that of a National Advisory Committee for Aeronautics

(NACA) airfoil (Figs. 1A and 2 A and B) (2, 3), leading it to develop negative pressure along most of its length (Figs. 3 and 4), like an airfoil (Fig. 1A) (4, 11). In both fish species, as in airfoils with an angle of attack to the flow (Fig. 1 A and C) (11, 12, 14–16), the region of positive pressure is not directly on the tip of the snout (Fig. 4 and *Movies S3* and *S4*). Instead, it oscillates to either side (Figs. 1A and 4 and *Movies S3* and *S4*), and the rest of the anterior body (segments 2 to 3, 10 to 40% L) solely experiences negative pressure (Figs. 3 and 4). This process is similar to leading-edge suction mechanics on airfoils at moderate angles of attack (Fig. 1C) (11, 12, 14–16). Our observations of negative pressure also match measurements by Dubois et al. (42, 44), who implanted pressure canulae under the skin of bluefish and found that negative pressure dominated much of the bluefish's length, leading to mean pressure profiles shaped similarly to those in Fig. 4 and suction-based thrust forces on the anterior body. Likewise, we find that negative pressure—arising from the airfoil-like shape, and placed far forward on the anterior body due to leading-edge suction mechanics—is positioned alongside forward-facing body surfaces and leads to small but significant, continuous thrust in segment 2 (10 to 20% L) (Figs. 3 and 5 A and B).

Similar pressure distributions have also been found in 3D computational fluid dynamics models of carangiform swimmers. Borazjani and Sotiropoulos (21) and Liu et al. (22) both documented negative-pressure regions along the anterior bodies in simulations of mackerel and crevalle jack, respectively, but they did not highlight the role of these negative pressures in thrust production. Even so, the presence of these mechanics across five phylogenetically distant species points to the ubiquity of airfoil-like thrust generation among carangiform swimmers.

This thrust production mechanism means that the anterior body produces less drag than it might otherwise, but it is still net drag producing. Dubois et al. (42–44), Anderson et al. (19), Borazjani and Sotiropoulos (21), and Liu et al. (22) all find that the anterior body produces net drag forces. Our work does not contradict these findings; indeed, we find that, on the anterior body, the magnitude of the negative-pressure thrust forces is smaller than the sum of drag forces (positive-pressure drag on the tip of the snout, segment 1, 0 to 10% L , and negative-pressure drag on the midbody, segment 3, 20 to 40% L) (Fig. 5 and *SI Appendix*, Fig. S2). However, the negative-pressure thrust on the anterior body (segments 1 to 4, 0 to 55% L) balances out a large fraction (45%) of this drag, causing the anterior body to produce much less net drag. Thus, we point to a more nuanced role for the anterior body during carangiform locomotion, as anterior-body thrust forces make up a substantial portion of the total thrust.

These thrust forces arise from very small movements of the anterior body (Fig. 2 A–D), and likely require little muscle activity. At low speeds, like in this study, trout do not activate red muscle anterior to 50% L (49), and neither do largemouth bass, a species closely related to bluegill sunfish (50). Thus, the small, mostly passive movement in the anterior body may allow this airfoil-like thrust production to be highly efficient.

This airfoil-like mechanism is different from the mechanism Gemmell et al. (25, 26) identified in larval lampreys, which also produce thrust due to negative pressure (Fig. 7). Larval lampreys swim in the anguilliform mode, which is characterized by large-amplitude undulations in the anterior regions of the body (Fig. 7) (17, 25, 27). Even among anguilliform swimmers, the larval lampreys studied by Gemmell et al. (25, 26) have particularly large anterior body movements (28). These undulations rotate the body surface, which accelerate the adjacent fluid, strengthen the fluid's vorticity, and generate large regions of negative pressure (Fig. 7A) (26, 51, 52). This negative pressure leads to suction-like thrust forces, which act continuously along much of the length of the body (Fig. 7A) (25, 26, 51, 52). In contrast,

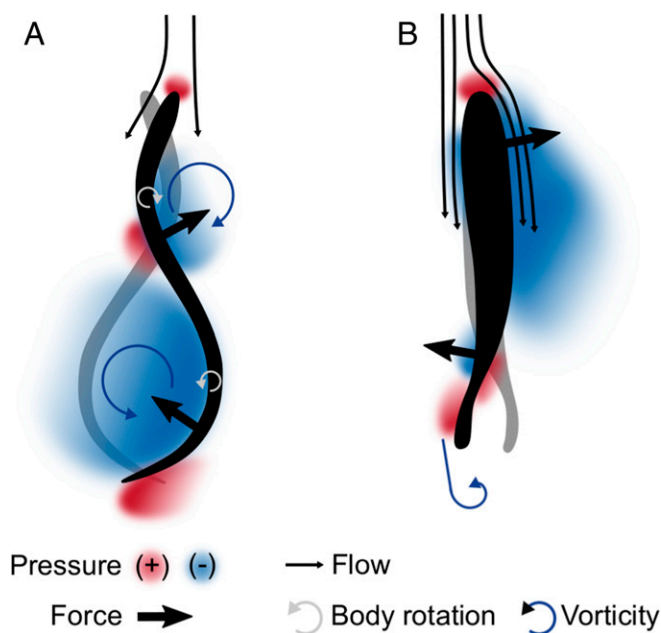


Fig. 7. Anterior body thrust for anguilliform and carangiform swimmers is based on different mechanics. Gray and black silhouettes show the motion of the body, and color indicates pressure. Anguilliform swimmers (A) produce negative-pressure thrust along the whole body using an undulatory pump mechanism, in which high-amplitude body movements suck fluid along the body. Anguilliform kinematics adapted from ref. 53. In contrast, carangiform swimmers (B) produce thrust on the anterior body through airfoil-like mechanics. For clarity, only negative-pressure thrust forces are shown.

bluegill and trout, which are carangiform swimmers, produce negative pressure locally on their anterior bodies due to their cross-sectional shape and small motions (Fig. 7B).

A growing body of work points to how different swimming modes and body shapes most likely confer different functional advantages (5–10). Detailed comparisons of force production by specific parts of the fish body like those performed here will allow us to finally test these hypotheses and, ultimately, arrive at a more complete understanding fish evolution and ecology. For example, we have long hypothesized that streamlined bodies like those of a tuna enable the fast, efficient swimming required of Pacific migrations. Here, we show that this body streamlining may contribute to the efficiency of thrust production. These fishes not only produce low drag but can also take advantage of the airfoil-like cross-section of their body and recoiling movements to produce thrust. Because the streamlined body cross-section and small anterior-body oscillations are very common in fishes, we suggest that this mechanism of producing thrust might be a general feature of swimming in many fish species.

Materials and Methods

Full details of the methods can be found in *SI Appendix, SI Materials and Methods*.

Experimental Procedures. Individual bluegill and brook trout swam at $2.5 L s^{-1}$ in a recirculating flume seeded with near-neutrally buoyant particles illuminated by horizontal laser light sheets from two sides. Fishes were filmed using two high-speed cameras (Photron Fastcam Mini AX50; $1,024 \times 1,024$ pixel resolution; $20\text{-}\mu\text{m}$ pixel size), which captured synchronized ventral and lateral view footage at 1,000 and 100 frames per second, respectively. Only sequences where the fish used steady, body-caudal fin swimming motions for at least 1.5 tailbeats cycles within the light sheet were processed. Video of three replicate swimming trials was collected for each individual.

Experiments were approved by the Harvard University Institutional Animal Care and Use Committee under protocol 20-03 (GVL).

Data Processing. Water velocity was calculated using particle image velocimetry in DaVis 8.2.2 (LaVision), with interrogation window sizes 32×32 pix and 16×16 pix, 50% overlap, and two passes at each window size (38).

Following our previously validated protocol (24), ventral outlines of the fish were manually digitized in ImageJ (NIH). Midlines were extracted automatically from these outlines using a custom Matlab 2015b (Mathworks) script. Midline kinematics (e.g., tailbeat period, frequency, lateral amplitude, and body angle) were calculated using a custom script in Python (version 2.7.11; Python Software Foundation; <https://www.python.org>) following Videler (29). We use the mathematical amplitude, the distance between the center line and maximum lateral excursion, which is half of the peak-to-peak lateral excursion, often referred to as “amplitude” in older works (1, 54). To facilitate comparisons across different parts of the fishes’ bodies, fishes were divided into seven body segments, which grouped together portions of the body with similar kinematics, body shape, and pressure gradients. Pressure and forces calculated below were averaged within segments.

Pressure distributions were calculated following Dabiri et al. (23) in Matlab using velocity data and outlines of the fishes’ bodies. We estimated forces using the procedure detailed in Lucas et al. (24). In brief, force magnitude was calculated as the product of pressure and surface area at a point in a calculation boundary drawn around the fish, where the area was the product of the distance between points in the horizontal plane and the fish’s body depth at those points. Force vectors were directed inward or outward based on the sign of the surrounding pressure. Our previous validations (24) indicate that, for fish-like swimmers, pressure effects dominate shear effects (e.g., skin friction), and that this 2D approach is robust to the out-of-plane flows around a fish [e.g., Liu et al. (22)], allowing for accurate estimation of forces through these procedures.

Statistics. Linear mixed effects models were developed following the standard practice outlined by Zuur et al. (55). For axial forces (C_{Fx}), two models were developed. The first compared the mean magnitudes of axial force subtypes and included four fixed effects, each with multiple levels: force type (thrust, drag), pressure type (positive, negative), species (bluegill, trout), and segment (1–7), and all interactions between these effects. The second model examined the means of total axial forces. Both this model and the model for mean lateral forces (C_{Fy}) included two fixed effects: species and segment, and their interaction. The model for efficiency included one fixed effect: species. In all models, individual was included as a random effect, and in force models, variance specifications accounted for heterogeneity (55, 56). ANOVA tests and post hoc pairwise comparisons were conducted to determine which effects significantly affected force coefficients. A false-discovery rate correction was applied to all post hoc results (57).

All statistics were performed in R (version 3.5.1; R Foundation for Statistical Computing; <https://www.r-project.org/>) using the nlme package (version 3.1–137; <https://cran.r-project.org/web/packages/nlme/index.html>), and marginal means were estimated for pairwise comparisons using the emmeans package (version 1.2.3; <https://cran.r-project.org/web/packages/emmeans/index.html>).

Data Availability. Fish swimming data files and statistical analyses are available from the “Surface pressure and swimming force calculation data for bluegill and trout steadily swimming at $2.5 L s^{-1}$ ” dataset on Harvard Dataverse available at <https://doi.org/10.7910/DVN/1SOLNG> (58). Scripts used for data processing are available at <https://github.com/kelseynlucas/Forces-on-carangiform-swimmers> (59).

ACKNOWLEDGMENTS. Thanks to Mariel Rosic for assistance with data collection; members of the G.V.L. laboratory for fish care; John Dabiri, Brad Gemmell, and Gary Lucas for technical assistance; Tyler Wise for sample data used to develop code; Steve Worthington and Kara Fellich for statistical advice; Paul Webb, Sean Colin, Elena Kramer, Pete Girguis, and members of the Girguis and E.D.T. laboratories for helpful discussions; Karthik Menon and Rajat Mittal for airfoil surface pressure data; and the anonymous reviewers whose feedback greatly improved the manuscript. This work was supported by an NSF Graduate Research Fellowship under Grant DGE-1745303 to K.N.L. and by NSF Grant Division of Integrative Organismal Systems Award 1652582 to E.D.T., and by the Office of Naval Research Multi-University Research Initiative Grant N000141410533 monitored by Dr. Bob Brizzolara to G.V.L. The funders had no role in study design, data collection and analysis, decision to publish, or preparation of the manuscript.

1. P. W. Webb, Hydrodynamic and energetics of fish propulsion. *Bull. Fish. Res. Board Can.* **190**, 1–156 (1975).
2. G. Cayley, *Aeronautical and Miscellaneous Note-Book (ca. 1799–1826) of Sir George Cayley; with An Appendix Comprising a List of Cayley Papers*, E. J. Hodgson, Ed. (W. Heffer and Sons, Cambridge, UK, 1933).
3. T. Von Kármán, *Aerodynamics: Selected Topics in the Light of Their Historical Development*, (Cornell University Press, Ithaca, NY, 1954).
4. S. Vogel, *Life in Moving Fluids: The Physical Biology of Flow*, (Princeton University Press, Princeton, ed. 2, 1994).
5. P. W. Webb, Body form, locomotion and foraging in aquatic vertebrates. *Am. Zool.* **24**, 107–120 (1984).
6. C. J. Fulton, D. R. Bellwood, Wave-induced water motion and the functional implications for coral reef fish assemblages. *Limnol. Oceanogr.* **50**, 255–264 (2005).
7. P. Domenici, B. G. Kapoor, *Fish Locomotion. An Eco-Ethological Perspective*, (CRC Press, Boca Raton, FL, 2010).
8. V. Astudillo-Clavijo, J. H. Arbour, H. López-Fernández, Selection towards different adaptive optima drove the early diversification of locomotor phenotypes in the radiation of Neotropical geophagine cichlids. *BMC Evol. Biol.* **15**, 77 (2015).
9. T. C. Haas, D. C. Heins, M. J. Blum, Predictors of body shape among populations of a stream fish (*Cyprinella venusta*, Cypriniformes: Cyprinidae). *Biol. J. Linn. Soc. Lond.* **115**, 842–858 (2015).
10. K. L. Feilich, Correlated evolution of body and fin morphology in the cichlid fishes. *Evolution* **70**, 2247–2267 (2016).
11. P. J. Pritchard, *Fox and McDonald's Introduction to Fluid Mechanics*, (John Wiley and Sons, Inc., Hoboken, NJ, ed. 8, 2011).
12. G. K. Batchelor, *An Introduction to Fluid Dynamics*, (Cambridge University Press, Cambridge, UK, 2000).
13. K. Menon, R. Mittal, Flow physics and dynamics of flow-induced pitch oscillations of an airfoil. *J. Fluid Mech.* **877**, 582–613 (2019).
14. G. T. Yates, "Hydromechanics of body and caudal fin propulsion" in *Fish Biomechanics*, P. W. Webb, D. Weihs, Eds. (Praeger Publishers, New York, 1983), pp. 177–213.
15. S. Narsipur, P. Hosangadi, A. Gopalathnam, J. R. Edwards, Variation of leading-edge suction at stall for steady and unsteady airfoil motions. *54th AIAA Aerospace Sciences Meeting* (January) (American Institute of Aeronautics and Astronautics, Reston, VA, 2016), p. 1354.
16. S. P. Sane, The aerodynamics of insect flight. *J. Exp. Biol.* **206**, 4191–4208 (2003).
17. J. Lighthill, *Mathematical Biofluidynamics*, (Society for Industrial and Applied Mathematics, Philadelphia, PA, 1975).
18. D. Weihs, P. W. Webb, "Optimization of locomotion" in *Fish Biomechanics*, P. W. Webb, D. Weihs, Eds. (Praeger Publishers, New York, 1983), pp. 339–371.
19. E. J. Anderson, W. R. McGillis, M. A. Grosenbaugh, The boundary layer of swimming fish. *J. Exp. Biol.* **204**, 81–102 (2001).
20. E. D. Tytell, Do trout swim better than eels? Challenges for estimating performance based on the wake of self-propelled bodies. *Exp. Fluids* **43**, 701–712 (2007).
21. I. Borazjani, F. Sotiropoulos, Numerical investigation of the hydrodynamics of carangiform swimming in the transitional and inertial flow regimes. *J. Exp. Biol.* **211**, 1541–1558 (2008).
22. G. Liu et al., Computational analysis of vortex dynamics and performance enhancement due to body–fin and fin–fin interactions in fish-like locomotion. *J. Fluid Mech.* **829**, 65–88 (2017).
23. J. O. Dabiri, S. Bose, B. J. Gemmill, S. P. Colin, J. H. Costello, An algorithm to estimate unsteady and quasi-steady pressure fields from velocity field measurements. *J. Exp. Biol.* **217**, 331–336 (2014).
24. K. N. Lucas, J. O. Dabiri, G. V. Lauder, A pressure-based force and torque prediction technique for the study of fish-like swimming. *PLoS One* **12**, e0189225 (2017).
25. B. J. Gemmill, S. P. Colin, J. H. Costello, J. O. Dabiri, Suction-based propulsion as a basis for efficient animal swimming. *Nat. Commun.* **6**, 8790 (2015).
26. B. J. Gemmill et al., How the bending kinematics of swimming lampreys build negative pressure fields for suction thrust. *J. Exp. Biol.* **219**, 3884–3895 (2016).
27. C. M. Breder, The locomotion of fishes. *Zoologica* **4**, 159–297 (1926).
28. A. D. McClellan, T. Pale, J. A. Messina, S. Buso, A. Shebib, Similarities and differences for swimming in larval and adult lampreys. *Physiol. Biochem. Zool.* **89**, 294–312 (2016).
29. J. J. Videler, *Fish Swimming*, (Springer Netherlands, Dordrecht, 1993).
30. G. V. Lauder, E. D. Tytell, "Hydrodynamics of undulatory propulsion" in *Fish Physiology*, R. E. Shadwick, G. V. Lauder, Eds. (Elsevier, Amsterdam, ed. 1, 2006), pp. 425–468.
31. T. J. Ehlinger, D. S. Wilson, Complex foraging polymorphism in bluegill sunfish. *Proc. Natl. Acad. Sci. U.S.A.* **85**, 1878–1882 (1988).
32. D. J. Ellerby et al., Assessing the ecological relevance of swimming performance traits: A case study of bluegill sunfish (*Lepomis macrochirus*). *Aquat. Ecol.* **52**, 311–322 (2018).
33. K. D. Fausch, R. J. White, Competition between brook trout (*Salvelinus fontinalis*) and brown trout (*Salmo trutta*) for positions in a Michigan stream. *Can. J. Fish. Aquat. Sci.* **38**, 1220–1227 (1981).
34. J. T. Petty, J. L. Hansbarger, B. M. Huntsman, P. M. Mazik, Brook trout movement in response to temperature, flow, and thermal refugia within a complex Appalachian riverscape. *Trans. Am. Fish. Soc.* **141**, 1060–1073 (2012).
35. A. Raj, A. Thakur, Fish-inspired robots: Design, sensing, actuation, and autonomy—a review of research. *Bioinspir. Biomim.* **11**, 31001 (2016).
36. R. W. Blake, Fish functional design and swimming performance. *J. Fish Biol.* **65**, 1193–1222 (2004).
37. M. Sfakiotakis, D. M. Lane, J. B. C. Davies, Review of fish swimming modes for aquatic locomotion. *IEEE J. Oceanic Eng.* **24**, 237–252 (1999).
38. M. Raffel et al., *Particle Image Velocimetry*, (Springer International Publishing, Cham, Switzerland, 2018).
39. T. N. Wise, M. A. B. Schwalbe, E. D. Tytell, Hydrodynamics of linear acceleration in bluegill sunfish, *Lepomis macrochirus*. *J. Exp. Biol.* **221**, jeb190892 (2018).
40. E. G. Drucker, G. V. Lauder, Locomotor forces on a swimming fish: Three-dimensional vortex wake dynamics quantified using digital particle image velocimetry. *J. Exp. Biol.* **202**, 2393–2412 (1999).
41. U. K. Müller, B. L. E. Van den Heuvel, E. J. Stamhuis, J. J. Videler, Fish footprints: Morphology and energetics of the wake behind a continuously swimming mullet (*Chelon labrosus* Risso). *J. Exp. Biol.* **200**, 2893–2906 (1997).
42. A. B. Dubois, G. A. Cavagna, R. S. Fox, Pressure distribution on the body surface of swimming fish. *J. Exp. Biol.* **60**, 581–591 (1974).
43. A. B. Dubois, C. S. Ogilvy, Forces on the tail surface of swimming fish: Thrust, drag and acceleration in bluefish (*Pomatomus saltatrix*). *J. Exp. Biol.* **77**, 225–241 (1978).
44. A. B. DuBois, G. A. Cavagna, R. S. Fox, Locomotion of bluefish. *J. Exp. Zool.* **195**, 223–235 (1976).
45. A. R. Blight, The muscular control of vertebrate swimming movements. *Biol. Rev. Camb. Philos. Soc.* **52**, 181–218 (1977).
46. U. K. Müller, J. Smit, E. J. Stamhuis, J. J. Videler, How the body contributes to the wake in undulatory fish swimming: Flow fields of a swimming eel (*Anguilla anguilla*). *J. Exp. Biol.* **204**, 2751–2762 (2001).
47. O. Akanyeti et al., Accelerating fishes increase propulsive efficiency by modulating vortex ring geometry. *Proc. Natl. Acad. Sci. U.S.A.* **114**, 13828–13833 (2017).
48. D. H. Kim, J. W. Chang, J. Chung, Low-Reynolds-number effect on aerodynamic characteristics of a NACA 0012 airfoil. *J. Aircr.* **48**, 1212–1215 (2011).
49. J. C. Liao, Neuromuscular control of trout swimming in a vortex street: Implications for energy economy during the Karman gait. *J. Exp. Biol.* **207**, 3495–3506 (2004).
50. B. Jayne, G. Lauder, Red muscle motor patterns during steady swimming in large-mouth bass: Effects of speed and correlations with axial kinematics. *J. Exp. Biol.* **198**, 1575–1587 (1995).
51. I. Borazjani, F. Sotiropoulos, Numerical investigation of the hydrodynamics of anguilliform swimming in the transitional and inertial flow regimes. *J. Exp. Biol.* **212**, 576–592 (2009).
52. S. Kern, P. Koumoutsakos, Simulations of optimized anguilliform swimming. *J. Exp. Biol.* **209**, 4841–4857 (2006).
53. A. Ayali, S. Gelman, E. D. Tytell, A. H. Cohen, Lateral-line activity during undulatory body motions suggests a feedback link in closed-loop control of sea lamprey swimming. *Can. J. Zool.* **87**, 671–683 (2009).
54. R. Bainbridge, The speed of swimming of fish as related to size and the frequency and amplitude of the tail beat. *J. Exp. Biol.* **35**, 109–133 (1957).
55. A. F. Zuur, E. N. Ieno, N. Walker, A. A. Saveliev, G. M. Smith, *Mixed Effects Models and Extensions in Ecology with R*, (Springer, New York, NY, 2009).
56. X. A. Harrison et al., A brief introduction to mixed effects modelling and multi-model inference in ecology. *PeerJ* **6**, e4794 (2018).
57. Y. Benjamini, Y. Hochberg, Controlling the false discovery rate: A practical and powerful approach to multiple testing. *J. R. Stat. Soc. B* **57**, 289–300 (1995).
58. K. N. Lucas, G. V. Lauder, E. D. Tytell, Surface pressure and swimming force calculation data for bluegill and trout steadily swimming at 2.5 L/s. Harvard Dataverse. <https://doi.org/10.7910/DVN/1SOLNG>. Deposited 16 March 2020.
59. K. N. Lucas, Forces-on-carangiform-swimmers. GitHub. <https://github.com/kelseynlucas/Forces-on-carangiform-swimmers>. Deposited 12 March 2020.

Supporting Information

Airfoil-like mechanics generate thrust on the anterior body of swimming fishes

Kelsey N. Lucas, George V. Lauder, and Eric D. Tytell

SI Materials and Methods

Fishes

Bluegill were captured by beach seine from White Pond, Concord, MA, USA, and were housed individually in 38 L tanks kept at 20°C. Bluegill were fed a combination of live worms and pellets. Brook trout were purchased from Blue Stream Aquaculture, West Barnstable, MA, USA, and were maintained in a 1500 L recirculating tank kept at 16°C. Trout were fed 3.5 mm high protein pellets daily (Keystone Hatcheries, Richmond, IL, USA). Fishes were kept on a 12-hour light: 12-hour dark photoperiod. All fish care and experimental protocols were approved by the Harvard University Institutional Animal Care and Use Committee under protocol 20-03 (G. Lauder).

Experimental setup and video collection

Experiments were performed in a 600 L recirculating flume with a 28 x 28 x 80 cm working area. Fish were blocked from drifting downstream outside the test area by a baffle and were encouraged to hold position in the center of the tank by the presence of vertical black strips of plastic clamped to the walls of the tank. Intake and outflow pipes from a chiller unit were positioned downstream of the test section. Water was chilled to 16°C during trout testing but was maintained at room temperature (20°C) for bluegill. Flow rates in the flume were controlled using a custom LabVIEW program (National Instruments Corp., Austin, TX, USA).

The flume was seeded with near-neutrally buoyant (density 1060 kg m⁻³) VESTOSINT 1164 white nylon 12 particles with an average diameter of 50 μm (Degussa Corporation, Piscataway, NJ, USA; now Evonik Industries AG, Essen, GER), and flow was pulsed to high

speeds periodically throughout testing to resuspend particles. Tracer particles were illuminated by two light sheets, one entering from either side of the tank and aligned to within 1 mm of each other, so as to eliminate shadows around the fish's body. Light sheets were produced by spreading the beams from two continuous wave 532 nm solid-state lasers (MGL-N-532A, OptoEngine, Midvale, UT, USA).

Before transfer to the test tank, each fish was measured for total length and then transferred to a small, rectangular container and photographed in lateral view with a scale bar. In the test tank, fish were given an acclimation window of 20 minutes to 12 hours prior to data collection, depending on the species, individual stress responses to handling, and response to the laser lights.

Individual swimming fish were filmed from two perspectives using two Photron Fastcam Mini AX50 (1024 x 1024 pixel resolution, 20 μm pixel size) high-speed video cameras. The first camera captured ventral view footage of the fish and surrounding flow off of a 45° mirror below the tank at 1000 frames per second (fps), and it was positioned to capture flow in the central region of the tank away from the walls, leading to images capturing a 26 x 26 cm space. The second camera was positioned adjacent to one of the lasers and aimed diagonally upstream. This camera filmed at 100 fps in sync with the ventral view camera and provided nearly-lateral view images of the fish, which were used to confirm that the fish was vertically centered in the laser light sheet during swimming trials selected for further processing. To ensure visibility of the fish, a red-pass filter (Schott Color Glass Filter, CG-OG-530-2.00-2.5, CVI Laser Corp., Albuquerque, NM, USA) was used on the lateral-view camera to reduce glare from the light sheet. Cameras ran continuously, and an end trigger was used to keep the last 12 seconds of video in memory for review and saving when the fish swam in the light sheet.

The criteria we used to select videos for processing are as follows. First, we required sequences where the fish used steady, body-caudal fin swimming motions for 1.5 tailbeat cycles. Although data would only be extracted from the duration of 1 tailbeat cycle during analysis, the extra 0.5 cycles were included to allow for a time buffer at the start and end of the sequence. We defined steady, body-caudal fin motion as the fish staying within 5 mm of its starting position (with one exception, where a 7 mm drift was permitted in order to maintain balanced experimental design) and not using pectoral fin beats. For each individual, footage of 3 replicate swimming trials was collected. Both fishes swam at 2.5 body lengths per second ($L s^{-1}$). Only

sequences where the whole body remained in the light sheet for the duration of a tailbeat were selected for further processing.

Calibration images were produced each time the cameras were moved by placing a plate with crosses marked on a 1 cm square grid in the test section at the depth of the laser sheet and taking photographs with the camera positioned beneath the tank.

Particle image velocimetry

Particle image velocimetry (PIV) analysis was conducted in DaVis 8.2.2 (LaVision GmbH, Goettingen, GER) (1–3). Cross-correlation was conducted with decreasing interrogation window sizes (32 x 32 and 16 x 16) and 50% overlap. Two passes were made at each window size. During postprocessing, vectors were deleted if their correlation value was <0.8 , and the empty spaces were filled by interpolation. This resulted in a 128 x 128 grid of velocity vectors. Due to the difficulty in automatically tracking fish fins, which appeared translucent and often in poor contrast to the background, fish were not masked during vector calculation, so vectors were calculated over the whole image, including inside of the fish's body. These internal vectors did not represent real flows. Smoothing regimes such as those used by Lucas et al. (4) consider the average flow among a vector's nearest neighbors (3). Because the fishes were not masked during processing, no smoothing regime was applied to prevent erroneous vectors calculated inside the fish's body from influencing real flow data.

Digitization for kinematics, body depth, and lateral area

Although ventral view videos were collected at 1000 fps for PIV analysis, our previous validations (4) indicated that major trends in forces on a swimming body are captured when pressure and force are calculated from velocity fields at 100 fps. For this reason, ventral outlines of the fish were manually digitized in ImageJ (NIH, Bethesda, MD, USA) in every tenth frame of ventral view video. In each outline, the first point was always placed on the anterior-most tip of the fish, and digitization thereafter proceeded clockwise, leading to outlines of 20-30 points. In addition to the kinematics tracking described below, ventral view outlines were also used in the calculation of pressure and forces.

Fish midlines were extracted automatically in a custom Matlab 2015b (Mathworks, Inc., Natick, MA, USA) script from manually-digitized ventral outlines. To do this, 20 points were

initialized inside the fish outline, evenly spaced on the x-axis between the manually-digitized anterior-most point, and an automatically identified tail tip. The tail tip was extracted based on curvature of the outline near points with the maximum x-coordinates, as fish always swam toward the left side of the screen. This initial straight line of 20 points was adjusted into a midline using a custom snake algorithm (5), which iteratively moved the 18 internal points in small steps in a direction chosen based on the weight of three tendencies: a tendency to move away from the edges of the fish outline, a tendency to stay near other points, and a tendency not to make a sharp angle with neighboring points. An arc-length interpolation was then used to generate a midline with 100 equally-spaced points.

Midlines kinematics were then calculated using a custom script in Python (version 2.7.11, Python Software Foundation; <https://www.python.org>). To do this, the midline was first smoothed using a quintic least-squares spline. Tailbeat period and frequency were then extracted from midline motion by tracking inflection points (positions of zero curvature) in the kinematic waveform traveling along the posterior half of the body following the methods described in Videler (6). Lateral amplitude of the kinematic waveform was calculated as the mean of peak lateral excursion of the midline, and the body angle – the angle the body made with the fish’s trajectory – was calculated as the tangential angle at each point on the midline.

In addition to the ventral outlines, a lateral view outline of each fish was manually digitized in ImageJ from the lateral view photographs taken before fishes were transferred into the test tank. The lateral area of a fish’s body was measured as the area enclosed by its manually-digitized lateral outline. Using the same initialization and snake algorithm process applied to make ventral view midlines above, lateral view midlines were generated. Body depth could then be automatically measured along lines drawn perpendicularly to the lateral view midline. This was accomplished by finding the distance between the points where the perpendicular lines intersected the dorsal and ventral outlines of the fish. On the caudal fin lobes, the body depth was the sum of distances between the dorsal and ventral outlines on each lobe. A body depth was calculated for each ventral view midline point, using the distance-along-body measure to relate the ventral and lateral view images.

Pressure and force calculation

Ultimately, velocity fields generated from PIV were used to calculate pressure distributions in the water around the fish's body using the Dabiri et al. (7) algorithm. The Dabiri et al. (7) algorithm has been validated against computational simulations of flow around a square cylinder and an anguilliform swimmer and in both cases, captures the major pressure gradients around these bodies. These pressure fields were then used to calculate forces acting on the fish's body following our previously-described protocols (4). Our earlier work (4) also details the validations of these pressure-based force calculation methods and shows that for fish-like swimming, the effects of shear forces are small enough that a pressure-based calculation provides an accurate estimate of swimming forces. Further, 3D bodies in flow will create flows that are inherently 3D, as illustrated for fish in Liu et al. (8). These flows include tip vortices and may not be captured with 2D quantification techniques for bodies with the aspect ratio of a fish (9, 10). Our validations also examine the influence of these effects for fish-like swimmers, and we find that this 2D approach is able to accurately reproduce the shape, timing, and magnitude of force-vs-time curves of fish-like swimmers (4).

The following paragraphs describe the pressure and force calculation process in more detail. Prior to these calculations, two more pieces of information were needed: specifications of where the fish's body was in the images and of where in space pressures should be extracted for force calculation.

First, the manually-digitized ventral outlines were used to create masks for use with the Dabiri et al. (7) pressure field calculator. These masks would blank out velocity vectors inside the fish's body and indicated to the algorithm the presence of a solid body (4, 7). To ensure that velocity vectors were enclosed in the narrow rostrum and caudal regions so that pressures would not be calculated through the fish's body, digitized outlines were adjusted – extending the rostrum by 0.5 mm and widening the caudal fin by 1.5 mm (0.75 mm on either side) (4) in Matlab 2015b.

Following the processing sequence detailed in Lucas et al. (4), we then generated boundaries which specified where around the fish's body we were interested in pressure magnitudes. These boundaries were set in Matlab 2015b as 198-point loops encircling the fish within 2.5 boundary-layer-widths of its surface, where pressure was defined and forces could be calculated (4, 7). For each frame of video that would be processed, the boundary was generated in three steps. First, pelvic fins were removed from the body outline, as well as pectoral fins for

trout (bluegill pectoral fins were held alongside the body). Paired fin outlines were required in the masks, as no flow information was available where these fins blocked the view of the laser light sheet, but for this same reason, forces could not be calculated directly on the portions of the body blocked from view by these fins. Then, an arc-length interpolation converted the remaining manually-digitized outline into an outline with 198 evenly-spaced points. Finally, this 198-point outline was expanded outward from the fish using another custom snake algorithm (5), which pushed the outline away from the fish while keeping boundary points relatively evenly spaced and the outline smooth.

We chose to calculate pressure in an 18 x 18 cm domain surrounding the fish, based on the following convergence analysis. Dabiri et al. (7) described in their supplemental material the need for care in choosing a domain size (length and width of the velocity field) because their algorithm calculates pressure along integration paths through the velocity field from the outer edge toward the center. Thus, domain size must compromise between keeping integration paths short to avoid accumulating error during pressure calculations and keeping the domain large enough so that the assumption that the pressure is zero on the edges of the domain was still valid. Following the protocol suggested by Dabiri et al. (7) to ensure the velocity field here met both of these criteria, a small sample of velocity fields were cropped to several dimensions (26, 22, 20, 18, 16, and 14 cm square fields and a rectangular 8 x 14 cm field cropped close to the fish's body). Then, the masks and these cropped velocity vector fields were then loaded into the Dabiri et al. (7) pressure algorithm to generate pressure fields. Pressure magnitudes on the calculation boundary and were plotted versus calculation boundary point to visualize fluctuations in the calculated pressure values induced by the changes in domain size. The 16, 18, and 20 cm square domains converged to similar calculated pressures around fish bodies – indicating minimal error induced by too large or too small domains – and so velocity fields were cropped to 18 x 18 cm windows centered around the fish during final pressure and force calculation.

After calculating pressure in this domain, we then estimated forces on the body. Force magnitudes were calculated at each point as the product of pressure and an area term, following the equations and procedure described in Lucas et al. (4). Pressures at force calculation boundary points located inside of paired fin outlines were estimated by linearly interpolating between pressures on either side of the fins. The area term for each calculation boundary point was the area of a rectangle whose width was the distance between calculation boundary points,

and whose length was the depth of the fish's body at the calculation boundary point. Body depth for a calculation boundary point was assumed to be the body depth at the nearest ventral view midline point. Pressure-based forces always act perpendicularly to a surface, so force vectors were always parallel with the normal vector at the corresponding calculation boundary points. Force vectors were directed inward or outward based on the sign of the surrounding pressure – positive pressure pushes on the body surface and directs force inward, while negative pressure pulls and directs force outward.

To enable comparison across swimming speeds and species, pressure and force were both normalized to non-dimensional pressure and force coefficients (C_p and C_F) as

$$C_p = \frac{p}{\frac{1}{2}\rho u^2} \quad (1)$$

$$C_F = \frac{F}{\frac{1}{2}\rho A u^2} \quad (2)$$

where C_p is pressure coefficient, p is pressure (Pa), C_F is force coefficient, F is force (N), ρ is the density of fresh water (1000 kg m⁻³), u is the swimming speed (m s⁻¹), and A is the lateral area of the fish's body (m²).

Because fish entered the light sheet and swam continuously starting at different points in a tailbeat cycle, all data were synchronized for comparisons based on the movement of the tip of the caudal fin. All time-series were reordered so that at time $t = 0$ s the tail tip was positioned at its maximum excursion to the right side of the body (as viewed in the videos). To allow for averaging across trials, all data were downsampled to 15 time points evenly distributed across the tail beat period. The shortest tailbeat period observed was 0.15 s. In addition, the right and left sides of the body experienced the same pressures and forces, but mirrored and at a lag of half of tailbeat cycle. Thus, data from the left side was mirrored and synchronized with data from the right side, leading to 2 time-series from every replicate tailbeat cycle which were averaged together. Reported pressure and force data therefore reflect what happens on one side of the body, unless otherwise indicated.

To facilitate comparisons across different parts of the fishes' bodies, fishes were divided into seven body segments. These segments were defined so as to keep lengths of segments as even as possible while grouping together portions of the body with similar kinematics, body shape, and pressure gradients.

All kinematic, mean pressure, and net force information were aggregated and synchronized for data reporting and statistical tests using a custom Python script.

Hydrodynamic efficiency

We approximate hydrodynamic Froude efficiency η , the ratio of useful power to total power (11), as $\eta = \sum_i (\mathbf{F}_{T,i} \cdot \mathbf{v}_i) / \sum_i |\mathbf{F}_i \cdot \mathbf{v}_i|$, where $\mathbf{F}_{T,i}$ is the thrust force vector, \mathbf{F}_i is the total force vector, and \mathbf{v}_i is the total velocity relative to the flow (including both side to side motion and the flow velocity) each on segment i .

Statistics

Statistical models were developed to quantify how pressure and force differs along the body among the two species. This led to the use of linear mixed effects models relating mean magnitude of axial force coefficient (C_{Fx}) subtypes to four effects, each with multiple levels: force type (thrust, drag), pressure type (positive, negative), species (bluegill, trout), and segment (1-7), and all interactions between these effects. Individual was included as a random effect to account for natural variation between individual fishes (12, 13). Because an examination of the residuals indicated that C_{Fx} data were heterogeneous, weights were applied to the model to allow for unequal variances among the grouping effects. Because all effects were categorical variables, unequal variance structures would allow for variance to differ between levels of one or more effects (12, 14). Appropriate variance structures were selected for each model by examining the variance and residuals at each level of each effect and constructing possible variance structures that described the unequal variance observed. The lowest Akaike Information Criterion score was used to select between models (12). After model selection, residuals were reexamined to verify that heterogeneity was no longer visible. This procedure follows the standard practice outlined by Zuur et al. (12). This led to a model allowing for variances to differ between all combinations of levels of species and body segment.

Fewer effects were of interest for comparisons of mean total axial force, as well as mean lateral force (C_{Fy}), coefficients leading to linear mixed effects models relating each of these to species, segment, and their interaction. As before, individual was included as a random effect (12, 13), and heterogeneity of variances were handled by introducing weight structures chosen through AIC scoring (12, 14). For total C_{Fx} , variance was allowed to differ between

combinations of species and segment. For C_{Fy} , variance was allowed to differ between body segments.

Efficiency models only had one fixed effect: species. Again, individual was included as a random effect (12, 13), but since variances were equal across species, no weight structure was needed.

Once appropriate models had been fit, ANOVA tests and post-hoc pairwise comparisons could be conducted to determine which effects significantly affected force coefficients. A false discovery rate correction was applied to all post-hoc results to correct for the likelihood that random, false significant differences would be detected (15).

All statistics were performed in R (version 3.5.1, R Foundation for Statistical Computing, Vienna, Austria; <https://www.r-project.org/>) using the nlme package (version 3.1-137, <https://CRAN.R-project.org/package=nlme>), and marginal means were estimated for pairwise comparisons using the emmeans package (version 1.2.3, <https://CRAN.R-project.org/package=emmeans>).

Data availability

Fish swimming data files and statistical analyses are available from the “Surface pressure and swimming force calculation data for bluegill and trout steadily swimming at 2.5 L/s” dataset on Harvard Dataverse available at <https://doi.org/10.7910/DVN/1SOLNG>. Scripts used for data processing are available at <https://github.com/kelseynlucas/Forces-on-carangiform-swimmers>.

SI References

1. Willert CE, Gharib M (1991) Digital particle image velocimetry. *Exp Fluids* 10(4):181–193.
2. Stamhuis EJ, Videler JJ (1995) Quantitative flow analysis around aquatic animals using laser sheet particle image velocimetry. *J Exp Biol* 294:283–294.
3. Raffel M, et al. (2018) *Particle Image Velocimetry* (Springer International Publishing, Cham) doi:10.1007/978-3-319-68852-7.
4. Lucas KN, Dabiri JO, Lauder G V. (2017) A pressure-based force and torque prediction technique for the study of fish-like swimming. *PLoS One* 12(12):e0189225.

5. Kass M, Witkin A, Terzopoulos D (1988) Snakes: Active contour models. *Int J Comput Vis* 1(4):321–331.
6. Videler JJ (1993) *Fish Swimming* (Springer Netherlands, Dordrecht) doi:10.1007/978-94-011-1580-3.
7. Dabiri JO, Bose S, Gemmell BJ, Colin SP, Costello JH (2014) An algorithm to estimate unsteady and quasi-steady pressure fields from velocity field measurements. *J Exp Biol* 217:331–336.
8. Liu G, et al. (2017) Computational analysis of vortex dynamics and performance enhancement due to body–fin and fin–fin interactions in fish-like locomotion. *J Fluid Mech* 829:65–88.
9. Raspa V, Ramanarivo S, Thiria B, Godoy-Diana R (2014) Vortex-induced drag and the role of aspect ratio in undulatory swimmers. *Phys Fluids* 26(4). doi:10.1063/1.4870254.
10. Yeh PD, Alexeev A (2016) Effect of aspect ratio in free-swimming plunging flexible plates. *Comput Fluids* 124:220–225.
11. Lighthill J (1975) *Mathematical Biofluidynamics* (Society for Industrial and Applied Mathematics, Philadelphia, PA).
12. Zuur AF, Ieno EN, Walker N, Saveliev AA, Smith GM (2009) *Mixed effects models and extensions in ecology with R* (Springer New York, New York, NY) doi:10.1007/978-0-387-87458-6.
13. Harrison XA, et al. (2018) A brief introduction to mixed effects modelling and multi-model inference in ecology. *PeerJ* 6:e4794.
14. Pinheiro JC, Bates DM (2000) *Mixed-Effects Models in S and S-PLUS* (Springer-Verlag, New York) doi:10.1007/b98882.
15. Benjamini Y, Hochberg Y (1995) Controlling the false discovery rate: A practical and powerful approach to multiple testing. *J R Stat Soc B* 57(1):289–300.

SI Figures

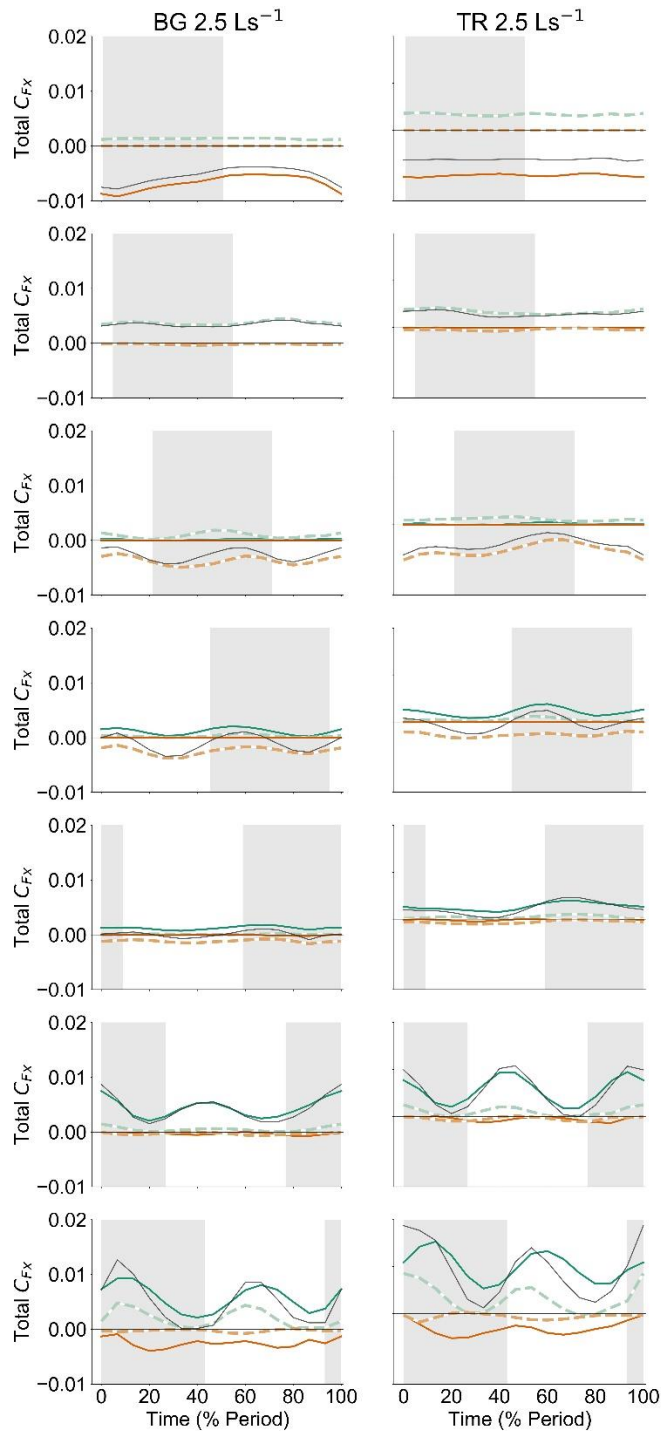


Fig. S1. Thrust and drag arise from both positive and negative pressure in time- and space-dependent patterns. Differences in timing of positive and negative pressure thrust forces on the caudal fin (segment 7, bottom row) control the timing of the peak in net thrust. The left column shows the total instantaneous force coefficients acting on the body (contrast with force coefficients from one side of the body in the main text) acting on bluegill (left column) and trout

(right column). Rows represent different body segments (see main text). The shaded region in the background indicates the times when the body segment moved from left to right, from peak amplitude to peak amplitude. Forces are colored by force type (green – thrust, orange – drag, grey – lateral component only) and pressure type (dark colors, solid lines – positive pressure, light colors, dashed lines – negative pressure), matching colors in the main text.

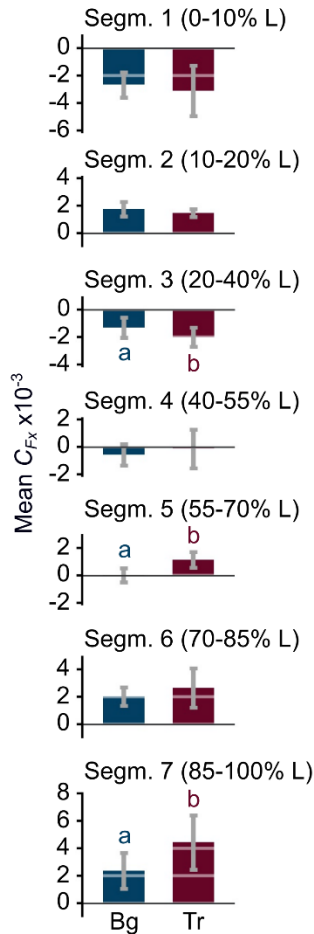


Fig. S2. Mean streamwise force coefficients in bluegill (Bg) and trout (Tr). Bars represent time-averaged mean forces on each body segment (Segm.) acting on one side of the body. Forces marked with different letters are significantly different from one another ($p < 0.05$). Transition from net drag to net thrust production occurs on the midbody, but in different segments for each species. The anterior body is net drag-producing, but thrust forces in Segm. 2 greatly reduce the impact of anterior-body drag.

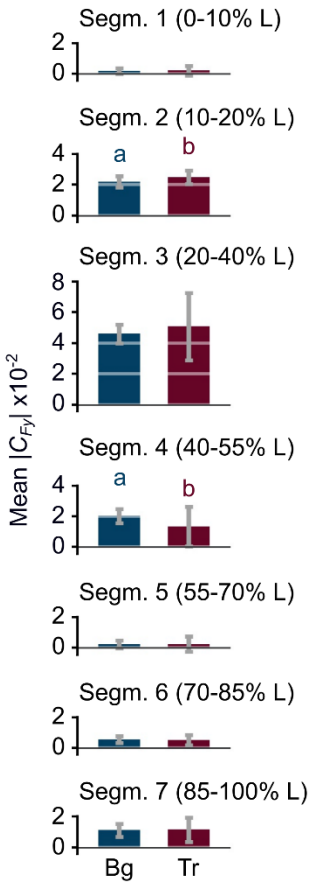


Fig. S3. Mean lateral force coefficients are similar between bluegill (Bg) and trout (Tr). The biggest difference occurs in segment 4, where trout have much lower lateral forces than bluegill. Rows represent different body segments (Segm., see main text). Forces marked with different letters are significantly different from one another ($p < 0.05$).

SI Movie Captions

Movie S1. Bluegill velocity field.

Movie S2. Trout velocity field.

Movie S3. Pressure distribution around bluegill.

Movie S4. Pressure distribution around trout.

Movie S5. Forces acting on the body of a freely-swimming bluegill. Forces are colored by force type (green – thrust, orange – drag, grey – lateral component only) and pressure type (dark colors – positive pressure, light colors – negative pressure), matching colors in the main text.

Movie S6. Forces acting on the body of a freely-swimming bluegill. Forces are colored by force type (green – thrust, orange – drag, grey – lateral component only) and pressure type (dark colors – positive pressure, light colors – negative pressure), matching colors in the main text.